Hyperentangled-state generation in nanophotonic periodically poled lithium niobate waveguides

Yanghe Chen,[1,3] Bo Ji,[1,3] Tengfei Wu,[4,†] and Guangqiang He[1,2,3,*]

[1] *State Key Laboratory of Advanced Optical Communication Systems and Networks, Department of Electronic Engineering, Shanghai Jiao Tong University, 200240 Shanghai, China*

[2] *State Key Laboratory of Precision Spectroscopy, East China Normal University, 200062 Shanghai, China*

[3] *SJTU Pinghu Institute of Intelligent Optoelectronics, Department of Electronic Engineering, Shanghai Jiao Tong University, 200240 Shanghai, China*

[4] *Science and Technology on Metrology and Calibration Laboratory, Changcheng Institute of Metrology & Measurement, Aviation Industry Corporation of China, 100095 Beijing, China*

(Received 12 September 2024; revised 26 November 2024; accepted 22 January 2025; published 12 February 2025)

Hyperentanglement is a promising resource in the realm of quantum communication, owing to its exploitation of multiple degrees of freedom. In this paper, we report the generation of a two-mode hyperentangled state using one nanophotonic periodically poled lithium niobate waveguide. Our approach encompasses the manipulation of polarization, energy-time, and quadrature amplitude-phase degrees of freedom. Theoretical calculations reveal that the magnitude of the Clauser-Horne-Shimony-Holt parameter $|S|$ can reach 2.375 even considering the multi-photon-pair generation effect, which is indicative of the entanglement in the polarization degree of freedom. Further analysis involved computing the joint spectral amplitude of the two-mode state, followed by Schmidt decomposition and Fourier transformation. The resulting joint uncertainty product $\Delta(\omega_s + \omega_i)\Delta(t_s - t_i) = 0.4113$, implying that high-quality energy-time entanglement is achieved. Notably, the von Neumann entropy S_r of our source reaches 0.192, confirming the presence of quadrature amplitude-phase entanglement within the generated state. Moreover, we theoretically apply our source in a free-space quantum key distribution system to demonstrate its potential to increase secret key rates. Our proposed scheme is an efficient and practical approach for facilitating high-capacity quantum communication systems.

DOI: 10.1103/PhysRevApplied.23.024030

I. INTRODUCTION

Hyperentanglement builds upon the concept of traditional entanglement by entangling particles in multiple degrees of freedom (DOFs) simultaneously [1]. This extension from singular to multiple entangled properties offers a plethora of potential advantages, including increased information capacity [2], enhanced security in quantum communication, improved robustness regarding environmental noise [3], and greater versatility in quantum protocols and algorithms [4,5]. By exploiting entanglement in multiple DOFs, hyperentanglement holds promise for revolutionizing quantum technologies, paving the way for more efficient quantum communication channels [6,7], more powerful quantum computing operations [8], and novel applications in quantum cryptography [9,10], quantum teleportation [11–13], and quantum metrology [14–16]. For example, multiple DOFs can be multiplexed on a single photon, transmitted through a quantum channel, and then demultiplexed onto different photons at the destination, which can significantly increase the transmission rate and channel capacity of quantum communication [17].

Previous efforts in hyperentanglement generation predominantly focused on harnessing hyperentanglement encoded in two DOFs. For instance, in 2015, Xie *et al.* [18] demonstrated the preparation of high-dimensional hyperentanglement using polarization and energy-time entanglement through a fiber Fabry-Pérot cavity and Hong-Ou-Mandel interference. Building upon this, in 2020, Hu *et al.* [19] achieved polarization-space hyperentanglement generation using a Sagnac interferometer, enabling hyperentanglement distribution over an 11 km fiber. Furthermore, the same Sagnac interferometer technique was adapted for the generation of polarization–time-bin hyperentanglement [20]. However, while two-DOF hyperentanglement has been extensively explored, the use of three DOFs holds promise for further increasing photon capacity and facilitating deterministic entanglement purification. Recent research by Zhao *et*

*Contact author: gqhe@sjtu.edu.cn
†Contact author: tengfei.wu@163.com

 © 2025 American Physical Society

al. [21] addresses this by designing generation protocols for three types of hyperentanglement encoded in three DOFs, leveraging practical coherent pulse sources. These include polarization–frequency-space, polarization-frequency–time-bin, and polarization–space–time-bin hyperentanglement. Nevertheless, these schemes rely on complex techniques such as Sagnac interferometry and time-reversed Hong-Ou-Mandel interference, which significantly increases the complexity of the experimental setup. Precise control over multiple quantum properties requires advanced optical systems and synchronization, making the experimental realization and stabilization of these states a daunting task.

To overcome the technical complexity for hyperentanglement preparation, we propose a hyperentangled-state generation scheme based on one nanophotonic periodically poled lithium niobate (PPLN) waveguide including polarization, energy-time, and quadrature amplitude-phase DOFs. By using a single waveguide that is periodically poled to address quasi-phase-matching conditions for three DOFs—that is, polarization, energy-time, and quadrature amplitude-phase (X-P) DOFs—our scheme significantly reduces the physical and operational complexity commonly associated with hyperentanglement setups. This approach eliminates the need for multiple disparate components to control each DOF separately, thereby reducing potential error sources and increasing the overall stability of the entanglement generation process. Moreover, lithium niobate waveguides are renowned for their electro-optic and nonlinear optical properties. By leveraging these characteristics, our scheme benefits from the high integration and miniaturization potential that nanophotonic devices offer. This compactness is crucial for scaling up quantum technologies and increases the feasibility of integrating hyperentangled-state generation into various quantum information processing systems, including those requiring portable and robust quantum communication links.

The application of our hyperentangled state in the quantum key distribution (QKD) system demonstrates its potential in high-dimensional encoding and multiplexing across multiple DOFs. By simultaneously encoding information in polarization, energy-time, and quadrature amplitude-phase DOFs, our hyperentangled state can significantly increase the secret key rate and efficiency of quantum communication. Additionally, the QKD protocol using the squeezed state (which is entangled in the quadrature amplitude-phase DOF) is more robust regarding channel excess noise and can tolerate higher channel loss, ensuring secure long-distance quantum communication [22]. The flexibility of hyperencoding allows information in multiple DOFs to independently generate secret keys, with operational errors in one DOF not affecting secret key generation in other DOFs.

This paper is organized as follows. In Sec. II, we introduce our compact hyperentanglement scheme, along with a detailed exposition of the fundamental parameters characterizing the designed lithium niobate waveguide. Section III provides our rigorous theoretical calculations on the magnitude of the Clauser-Horne-Shimony-Holt (CHSH) parameter $|S|$, joint uncertainty product $\Delta(\omega_s+\omega_i)\Delta(t_s-t_i)$, and squeezing degree S_r to confirm the entanglement in polarization, energy-time, and quadrature amplitude-phase DOFs, respectively. In Sec. IV, we demonstrate the application of our hyperentangled state in a theoretical free-space QKD system. Section V provides a conclusion and outlook.

II. HYPERENTANGLED TWO-MODE SOURCE SCHEME

In our scheme, we use one nanophotonic PPLN waveguide to implement hyperentanglement across three DOFs, as shown in Fig. 1(a), with its cross section depicted in Fig. 1(b). Fabricated using a 0.6-μm-thick z-cut lithium niobate crystal film, the waveguide leverages the material's excellent electro-optic properties, high nonlinear coefficients, and wide transparency range. A trapezoidal center section of the waveguide, measuring 8 mm in length, efficiently transmits pump, signal, and idler light, optimizing the phase-matching conditions necessary for effective frequency conversion processes. Detailed simulations provide effective refractive index dispersion curves for both ordinary light and extraordinary light, as illustrated in Fig. 1(c).

The input pump light wavelength λ_p used is 780 nm, corresponding to angular frequency $\omega_p = 2\omega_0 = 2.41 \times 10^{15}$ rad/s, where ω_0 represents the center frequency of the signal and idler light generated by spontaneous parametric down-conversion (SPDC). The wave vector is given by the equation $k(\omega) = n(\omega) \times \omega/c$, where $n(\omega)$ is the effective refractive index and c is the speed of light. The wave vector values are given as $k_o(2\omega_0) = 1.74 \times 10^7\ \mathrm{m}^{-1}$ for the pump light, $k_o(\omega_0) = 7.57 \times 10^6\ \mathrm{m}^{-1}$ for the ordinary light, and $k_e(\omega_0) = 8.02 \times 10^6\ \mathrm{m}^{-1}$ for the extraordinary light. To compensate for wave vector mismatch when the signal and idler light frequencies are equal, single-period poling is used. The wave vector mismatch is calculated as $k_{\mathrm{PP}} = k_o(2\omega_0) - k_o(\omega_0) - k_e(\omega_0) = 1.82 \times 10^6\ \mathrm{m}^{-1}$. According to the quasi-phase-matching theory, $k_{\mathrm{PP}} = 2\pi/\Lambda$, leading to a calculated poling period Λ of 3.45 μm.

The generated hyperentangled state across the three DOFs can be expressed as the tensor product of the polarization-frequency hyperentanglement state $|\psi\rangle_1$ and the two-mode squeezed vacuum state $|\psi\rangle_2$:

$$|\psi\rangle = |\psi\rangle_1 \otimes |\psi\rangle_2. \tag{1}$$

The two-mode squeezed vacuum state $|\psi\rangle_2$ can be expanded with use of the two-mode photon number state

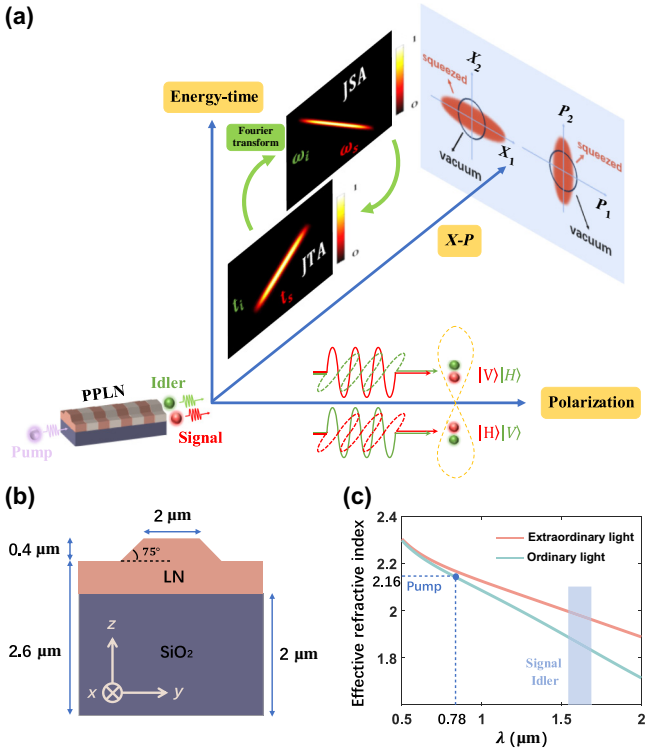

FIG. 1. (a) Generation of photon pairs entangled simultaneously in three degrees of freedom: polarization, energy-time, and quadrature amplitude-phase. (b) Cross section of the PPLN waveguide, with its dispersion curve for both extraordinary light and ordinary light shown in (c). LN, lithium niobate.

as

$$|\psi\rangle_2 = \sum_k C_{k,k}|k,k\rangle, \quad C_{k,k} = \frac{1}{\cosh r}(-e^{i\theta}\tanh r)^k, \quad (2)$$

where r and θ are the squeezed amplitude and phase, respectively.

We can derive the polarization-frequency hyperentanglement state $|\psi\rangle_1$ through a general method for the SPDC process. The nonlinear interaction Hamiltonian describes the interaction in the PPLN waveguide as follows [23]:

$$\hat{H}_{\rm int}(t) \propto \epsilon_0 \int \mathrm{d}^3\mathbf{r} \sum_{\alpha,\beta,\gamma} \chi^{(2)}_{\alpha,\beta,\gamma}(\mathbf{r})\mathbf{E}^+_{p,\gamma}(\mathbf{r},t) \times \hat{\mathbf{E}}^-_{s,\alpha}(\mathbf{r},t)\hat{\mathbf{E}}^-_{i,\beta}(\mathbf{r},t) + \text{H.c.}, \quad (3)$$

where $\chi^{(2)}_{\alpha,\beta,\gamma}(\mathbf{r})$ is the second-order nonlinear susceptibility tensor, $\mathbf{E}^+_{p,\gamma}$ is the positive frequency component of the pump electric field, and $\hat{\mathbf{E}}^-_{s,\alpha}$ and $\hat{\mathbf{E}}^-_{i,\beta}$ are the negative frequency components of the signal and idler fields, respectively. The term H.c. denotes the Hermitian conjugate, representing the inverse process of SPDC. The time evolution of the quantum state in the interaction picture is given by

$$|\psi(t\to+\infty)\rangle_1 \approx |0\rangle - \frac{i}{\hbar}\int_{-\infty}^{+\infty}\hat{H}_{\rm int}(t)|0\rangle \mathrm{d}t. \quad (4)$$

The generated two-mode state, considering the dominant contributions, is represented as [24]

$$\begin{aligned}|\psi\rangle_1 \propto \iint \mathrm{d}\omega_s \mathrm{d}\omega_i \{&A(\omega_s,\omega_i)|s,o,\omega_s\rangle|i,e,\omega_i\rangle \\ &+ B(\omega_s,\omega_i)|s,e,\omega_s\rangle|i,o,\omega_i\rangle \\ &+ C(\omega_s,\omega_i)|s,o,\omega_s\rangle|i,o,\omega_i\rangle \\ &+ D(\omega_s,\omega_i)|s,e,\omega_s\rangle|i,e,\omega_i\rangle\}, \end{aligned} \quad (5)$$

where $|s/i,o/e,\omega_s/\omega_i\rangle = \hat{a}^\dagger_{s/i,o/e,\omega_s/\omega_i}|0\rangle_{s/i}$. The joint spectral amplitude (JSA) for the process $o \to o+e$ is defined as

$$A(\omega_s,\omega_i) = \sqrt{\omega_s\omega_i}A_{ov}A_p(\omega_s+\omega_i)A_{JPS}, \quad (6)$$

where A_{JPS} and the overlap integral A_{ov} for the process $o \to o+e$ are given by

$$\begin{aligned} A_{JPS} &= \frac{e^{[i(k_p-k_{s,o}-k_{i,e})-\alpha_p]L}-1}{i(k_p-k_{s,o}-k_{i,e})-\alpha_p}, \\ A_{ov} &= \frac{\sqrt{n_{gs}n_{gi}}\int_\Omega \mathrm{d}^3\mathbf{r}\sum_{\alpha\beta\gamma}\chi^{(2)}_{\alpha\beta\gamma}e_{p,\gamma}e^*_{s,o,\alpha}e^*_{i,e,\beta}}{\sqrt{\int_\Omega \mathrm{d}^3\mathbf{r}\mathbf{d}_s\cdot\mathbf{e}^*_s\int_\Omega \mathbf{d}_i\cdot\mathbf{e}^*_i}}. \end{aligned} \quad (7)$$

$B(\omega_s,\omega_i)$, $C(\omega_s,\omega_i)$, and $D(\omega_s,\omega_i)$ can be obtained by the same method. Considering the type-II phase matching condition we used, we can assume that $C(\omega_s,\omega_i) \approx D(\omega_s,\omega_i) \approx 0$, and thus the resulting two-mode state $|\psi\rangle_1$ can be written as

$$\begin{aligned}|\psi\rangle_1 = \iint \mathrm{d}\omega_s \mathrm{d}\omega_i \{&A(\omega_s,\omega_i)|s,o,\omega_s\rangle|i,e,\omega_i\rangle \\ &+ B(\omega_s,\omega_i)|s,e,\omega_s\rangle|i,o,\omega_i\rangle\}. \end{aligned} \quad (8)$$

III. QUANTUM CHARACTERISTICS OF THE GENERATED STATE

A. Polarization entanglement

In Sec. II, we made the frequencies of the signal light and the idler light equal ($\omega_s = \omega_i = \omega_0$) in order to calculate the poling period Λ. However, if we change ω_s to be $\omega_0 - (\Delta\omega/2)$ and ω_i to be $\omega_0 + (\Delta\omega/2)$, the SPDC process can occur with efficiency $\mathrm{sinc}^2(\Delta kL/2)$, where $\Delta\omega$ is the difference between the signal and idler light frequencies, Δk is the wave vector mismatch, and L is the waveguide length [25]. Here, the signal light frequency is

on the left side of ω_0, and the idler light frequency is on the right side of ω_0. The wave vector mismatch is given by

$$\Delta k = k_p - k_m\left(\omega_0 - \frac{\Delta\omega}{2}\right) - k_n\left(\omega_0 + \frac{\Delta\omega}{2}\right), \quad (9)$$

where $m, n = o, e$ denote the polarization states of the signal and idler light. When the wave vector mismatch is not fully compensated, the efficiency of the nonlinear process decreases. In our z-cut waveguide, there are two modes, the transverse electric (TE) mode and the transverse magnetic (TM) mode, both of which are associated with the electric polarization direction and which correspond to extraordinary light (TE mode) and ordinary light (TM mode), respectively. Because of the possibility of there being two modes in our waveguide, the generated photons (signal and idler) may exist in the TM mode or the TE mode, resulting in four possible cases: (1) $o_p \to e_s + o_i$; (2) $o_p \to o_s + e_i$; (3) $o_p \to o_s + o_i$; (4) $o_p \to e_s + e_i$. However, these four processes have different conversion efficiencies, and Fig. 2 shows conversion efficiencies corresponding to type-II and type-I phase matching conditions. When the frequency spacing of the two photons reaches 192 GHz for the type-II SPDC process, the conversion efficiency drops to zero, which defines the bandwidth of the quantum entanglement source. In the type-I SPDC process, the value of the conversion efficiency function tends to zero, leading to the assumption that the type-I SPDC process does not occur. The type-II SPDC process includes two cases: $o \to o + e$ and $o \to e + o$, both of which have nearly identical conversion efficiency functions. This result means that when the signal photon is in the TM mode, the idler photon is in the TE mode ($o_p \to o_s + e_i$); when the signal photon is in

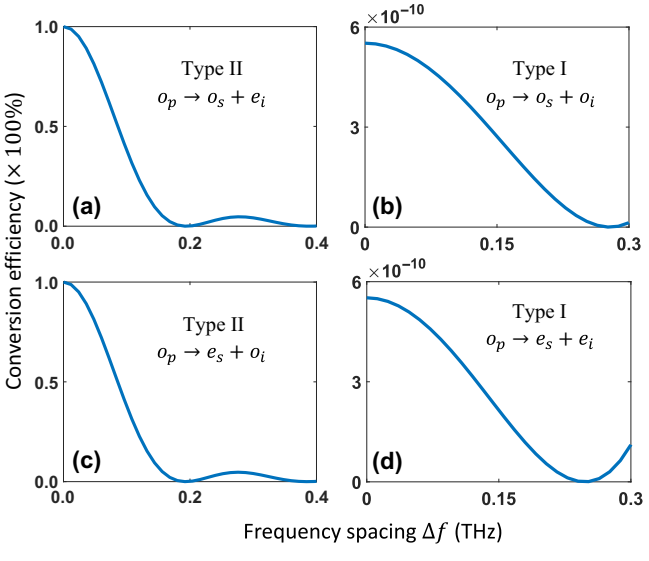

FIG. 2. Conversion efficiency curves for (a),(c) type-II phase matching conditions and (b),(d) type-I phase matching conditions.

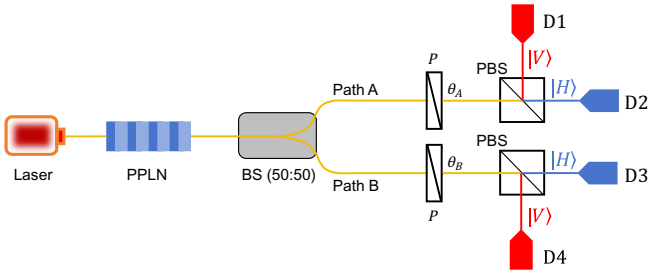

FIG. 3. Simplified method for polarization entanglement validation. BS, beam splitter; P, polarizer; PBS, polarizing beam splitter.

the TE mode, the idler photon is in the TM mode ($o_p \to e_s + o_i$), and both processes can exist simultaneously and occur approximately with equal probability, resulting in a maximally entangled Bell state in the polarization DOF.

We can verify polarization entanglement using the CHSH inequality, whereby the magnitude of the CHSH parameter $|S| > 2$ indicates the existence of polarization entanglement [26]. A simplified validation method is shown in Fig. 3, where the generated polarization-entangled state travels along two separate spatial paths through a 50:50 beam splitter. This state is then manipulated with the use of two polarization controllers, each rotating the polarization vector by angles θ_A and θ_B. Subsequently, the photons from both paths are directed through ideal polarizing beam splitters: horizontally polarized photons are directed toward detectors D2 and D3, while vertically polarized photons are directed toward detectors D1 and D4. Note that the lithium niobate waveguide has the potential to generate any number of photon pairs, while the multi-photon-pair generation effect will reduce the entanglement degree in the polarization DOF. The two-mode squeezed state after the 50:50 beam splitter can be expressed as [27]

$$|\psi\rangle_2' = \frac{1}{\cosh(r)} e^{-\tanh(r)(\hat{a}_H^\dagger \hat{b}_V^\dagger - \hat{a}_V^\dagger \hat{b}_H^\dagger + i\hat{a}_H^\dagger \hat{a}_V^\dagger + i\hat{b}_H^\dagger \hat{b}_V^\dagger)/2}|0\rangle, \quad (10)$$

where r is the squeezed coefficient. The polarization rotations in paths A and B apply the transformation to the operators, which can be expressed as

$$\begin{aligned}
\hat{a}_H^\dagger &\to \cos\theta_A \hat{a}_H^\dagger + \sin\theta_A \hat{a}_V^\dagger, \\
\hat{a}_V^\dagger &\to \cos\theta_A \hat{a}_V^\dagger - \sin\theta_A \hat{a}_H^\dagger, \\
\hat{b}_H^\dagger &\to \cos\theta_B \hat{b}_H^\dagger + \sin\theta_B \hat{b}_V^\dagger, \\
\hat{b}_V^\dagger &\to \cos\theta_B \hat{b}_V^\dagger - \sin\theta_B \hat{b}_H^\dagger.
\end{aligned} \quad (11)$$

Substituting Eq. (11) into Eq. (10), we can write the two-mode squeezed state $|\psi\rangle_2''$ before the detectors as

$$|\psi\rangle_2'' = \frac{1}{\cosh(r)} e^{-\tanh(r)\cos(\theta_A-\theta_B)\left(\hat{a}_H^\dagger \hat{b}_V^\dagger - \hat{a}_V^\dagger \hat{b}_H^\dagger\right)/2} \times e^{-\tanh(r)\sin(\theta_A-\theta_B)\left(\hat{a}_H^\dagger \hat{b}_H^\dagger + \hat{a}_V^\dagger \hat{b}_V^\dagger\right)/2} \times e^{i\tanh(r)\sin(2\theta_A)\left(\hat{a}_H^{\dagger 2} - \hat{a}_V^{\dagger 2}\right)/4} \times e^{i\tanh(r)\sin(2\theta_B)\left(\hat{b}_H^{\dagger 2} - \hat{b}_V^{\dagger 2}\right)/4} \times e^{-i\tanh(r)\left[\cos(2\theta_A)\hat{a}_H^\dagger \hat{a}_V^\dagger + \cos(2\theta_B)\hat{b}_H^\dagger \hat{b}_V^\dagger\right]/2}|0\rangle. \quad (12)$$

Using the Husimi-Kano function to calculate the coincidence rate, we can derive the magnitude of the CHSH parameter $|S|$ when considering the multi-photon-pair generation effect [27]:

$$|S| = 2\sqrt{2}\frac{\cosh^2(r)}{2\cosh(2r)-1}. \quad (13)$$

From Eq. (13), we can see that when $r \to 0$, which means $|\psi\rangle_2$ contains mainly the biphoton state $|1,1\rangle$, $|S| \to 2\sqrt{2}$, corresponding to the ideal situation in our scheme. Besides, when r increases to 0.39, $|S|$ decreases to 2; when $r > 0.39$, $|S| < 2$, implying there is no entanglement in the polarization DOF.

In our scheme, the squeezed coefficient $r = 0.258$ (see details in Sec. III C), and $S = 2.375$, indicating that our source still remains entangled in the polarization DOF even considering the multi-photon-pair generation effect. We note that polarization entanglement and X-P entanglement have a mutually conflicting relationship—that is, high polarization entanglement will result in low X-P entanglement, and vice versa. Therefore, a compromise r needs to be designed to ensure entanglement on both DOFs simultaneously.

B. Energy-time entanglement

The JSA $A(\omega_s, \omega_i)$ and the joint temporal amplitude (JTA) $\tilde{A}(t_s, t_i)$ can be used to explore two-photon-pair entanglement in the energy-time DOF. The wavelength of the input pump light is 780 nm. We assume that the pump light follows a Gaussian distribution, so the JSA [shown in Fig. 5(b)] is determined mainly by the phase-matching intensity [shown in Fig. 5(a)]. A Schmidt decomposition can be performed on $A(\omega_s, \omega_i)$ [28]:

$$A(\omega_s, \omega_i) = \sum_{n=1}^{N} \sqrt{\lambda_n}\psi_n(\omega_s)\phi_n(\omega_i), \quad (14)$$

where λ_n are Schmidt coefficients, and $\psi_n(\omega_s)$ and $\phi_n(\omega_i)$ are orthogonal functions in the Hilbert space. These are solutions of the following eigenvalue equations:

$$\int K_1(\omega, \omega')\psi_n(\omega')\mathrm{d}\omega' = \lambda_n\psi_n(\omega), \quad \int K_2(\omega, \omega')\phi_n(\omega')\mathrm{d}\omega' = \lambda_n\phi_n(\omega), \quad (15)$$

where $K_1(\omega, \omega') \equiv \int A(\omega, \omega_2)A^*(\omega', \omega_2)d\omega_2$ and $K_2(\omega, \omega') \equiv \int A(\omega_1, \omega)A^*(\omega_1, \omega')d\omega_1$. Therefore, the degree of entanglement is measured with the use of the entropy of entanglement S and the effective Schmidt rank K:

$$S = -\sum_{n=1}^{N} \lambda_n \log_2 \lambda_n, \quad (16)$$

$$K = \frac{\left(\sum_{n=1}^{N} \lambda_n\right)^2}{\sum_{n=1}^{N} \lambda_n^2}. \quad (17)$$

$S > 0$ and $K > 1$ indicate the presence of entanglement, with larger values signifying a higher degree of entanglement. The first ten Schmidt coefficients, arranged from largest to smallest, are shown in Fig. 6(a). The resulting effective Schmidt rank $K = 3.6532 > 1$, and S converges to 2.1276 [shown in Fig. 6(b)], confirming the continuous frequency entanglement property of our source. The first four basis functions of Eq. (15) are plotted in Fig. 4.

The JTA can be derived through the Fourier transform [29]:

$$\tilde{A}(t_s, t_i) = \mathcal{F}[A(\omega_s, \omega_i)] = \iint d\omega_i d\omega_s A(\omega_i, \omega_s)e^{i\omega_i t_i}e^{i\omega_s t_s}; \quad (18)$$

the simulation result is plotted in Fig. 5(c). We can also perform the Schmidt decomposition on the JTA and calculate its entanglement degree. The Schmidt coefficients λ_n derived from the JTA are identical to those obtained from the JSA, meaning that $S = 2.1276$ and $K = 3.6532$ are the same as for the JSA. These confirm that the two-photon state generated by our entangled source is also continuously time-entangled.

The joint uncertainty product Δ_{un}, which is the product of the standard deviation of the sum of the frequencies $\Delta(\omega_s + \omega_i)$ and the standard deviation of the

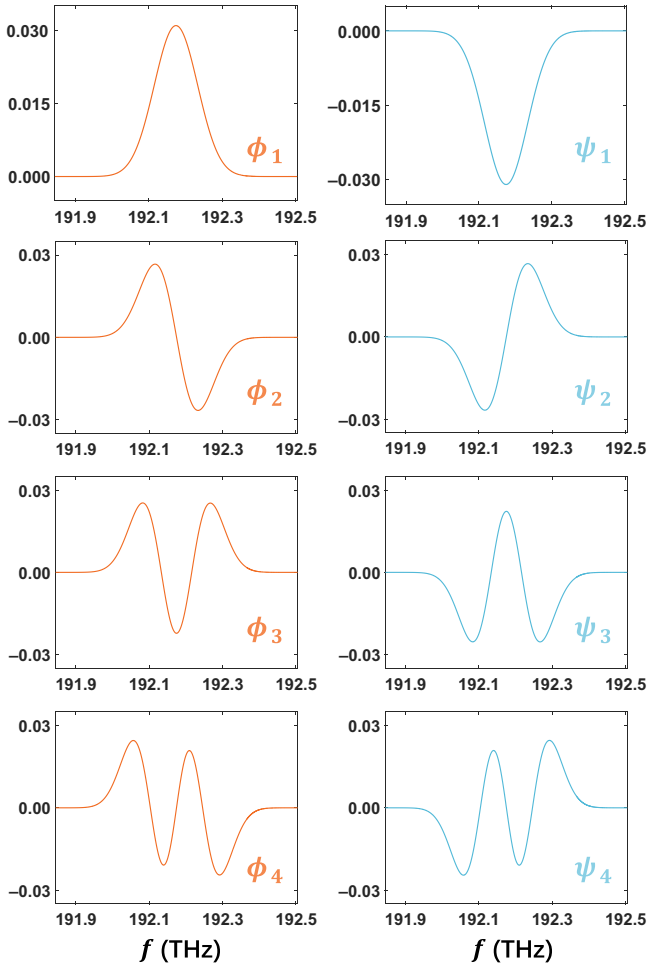

FIG. 4. First four basis functions for ϕ_n (left column) and ψ_n (right column), respectively.

difference in the arrival times $\Delta(t_s - t_i)$, serves as a measure of energy-time entanglement [30]. A joint uncertainty product less than 1 is direct evidence of energy-time entanglement between the signal photon and the idler photon [29,31]. From the JSA and the JTA we obtained, the two standard deviation values can be calculated, $\Delta(\omega_s + \omega_i) = 9.0358 \times 10^{10}\,\mathrm{s}^{-1}$ and $\Delta(t_s - t_i) = 4.5520 \times 10^{-12}$ s, leading to the joint uncertainty product $\Delta_{\mathrm{un}} = \Delta(\omega_s + \omega_i)\Delta(t_s - t_i) = 0.4113$. This demonstrates the energy-time entanglement property of the generated two-mode state, providing direct evidence of the entangled nature in both the energy domain and the time domain.

Typically, the length of nonlinear crystals can significantly affect phase matching and the JSA of the generated photons, thereby impacting the degree of energy-time entanglement. To investigate this issue, we change the length of the waveguide L to 2, 5, and 15 mm, and then simulate the corresponding JSA distribution, as shown in Figs. 5(d)–5(f), respectively. Our findings indicate that the bandwidth of the generated photons narrows as L increases. Besides, we also calculate the joint uncertainty product Δ_{un} when L changes. From Figs. 5(d)–5(f), it is observed that by appropriately reducing L, we can increase energy-time entanglement. However, excessive reduction or increase in L will decrease entanglement. This is because high L will destroy the phase-matching conditions of the SPDC process, while very low L results in insufficient interaction time, both of which will degrade the quality of entanglement. Perhaps the optimal L could be determined through inverse design [32] or machine learning algorithms [33] in the future.

C. *X*-*P* entanglement

Quadrature amplitude ($\hat{X}$) and quadrature phase ($\hat{P}$) are fundamental components in the quantum description of the electromagnetic field, representing the in-phase and out-of-phase parts of the field, respectively. In the field of quantum optics, the position operator and the momentum operator are defined as

$$\hat{X}_{1,2} = \frac{1}{\sqrt{2}}(\hat{a}_{1,2} + \hat{a}_{1,2}^{\dagger}), \quad \hat{P}_{1,2} = \frac{-i}{\sqrt{2}}(\hat{a}_{1,2} - \hat{a}_{1,2}^{\dagger}), \tag{19}$$

where $\hat{a}_{1,2}$ and $\hat{a}_{1,2}^{\dagger}$ are the generation operator and the annihilation operator of two particles, respectively. Considering the continuous frequency entanglement property of our source, the nonlinear part of the Hamiltonian in our lithium niobate waveguide can be described as

$$\begin{aligned} \hat{H}_{\mathrm{int}} &= \gamma \left(\iint A(\omega_s, \omega_i)\hat{a}_s^{\dagger}\hat{a}_i^{\dagger}\mathrm{d}\omega_s\mathrm{d}\omega_i + \mathrm{H.c.} \right), \\ \gamma &= \hbar\alpha_p g, \\ g &= 2\epsilon_0\chi^{(2)}\sqrt{\frac{\hbar\omega_s\omega_i\omega_p}{8\epsilon_s\epsilon_i\epsilon_p S_{\mathrm{eff}}L}}, \end{aligned} \tag{20}$$

where $\hat{a}_s^{\dagger}$ ($\hat{a}_i^{\dagger}$) is the creation operator for signal (idler) modes, γ is the nonlinear interaction strength, α_p denotes the square root of the pump photon number, g represents the single-photon coupling rate, ϵ_0 is the vacuum permittivity, L is the length of the lithium niobate waveguide, $\chi^{(2)}$ is the second-order nonlinear coefficient, S_{eff} is the spot area of the pump light, ϵ_k ($k = s, i, p$) is the permittivity for the optical field and H.c. is the Hermitian conjugate. Using the Schmidt decomposition mentioned in the previous subsection, that is, $A(\omega_s, \omega_i) = \sum_{n=1}^{N}\sqrt{\lambda_n}\psi_n(\omega_s)\phi(\omega_i)$, we can rewrite Eq. (20) as

$$\hat{H}_{\mathrm{int}} = \gamma \sum_n (\sqrt{\lambda_n}\hat{S}_n^{\dagger}\hat{I}_n^{\dagger} + \mathrm{H.c.}), \tag{21}$$

where

$$\hat{S}_n^{\dagger} = \int \psi_n(\omega_s)\hat{a}_s^{\dagger}\mathrm{d}\omega_s, \quad \hat{I}_n^{\dagger} = \int \phi_n(\omega_i)\hat{a}_i^{\dagger}\mathrm{d}\omega_i. \tag{22}$$

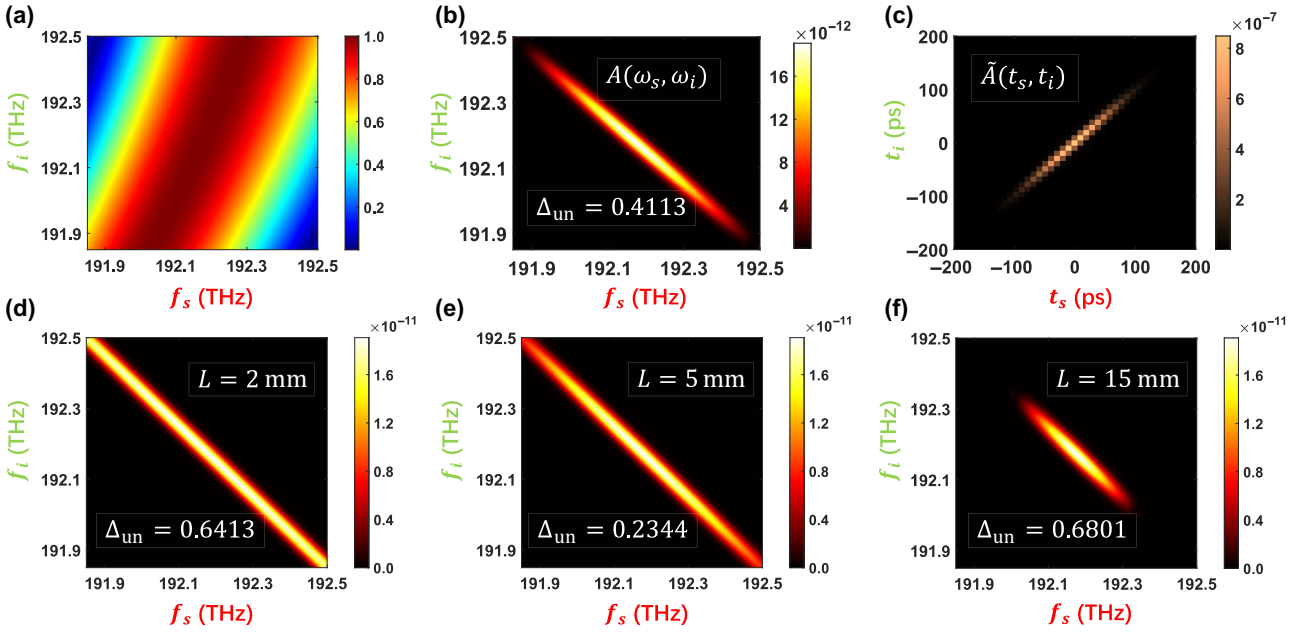

FIG. 5. (a) Phase-matching intensity distribution of the SPDC process in the PPLN waveguide. (b) JSA distribution and (c) JTA distribution of our generated state through the PPLN when the length of the waveguide $L = 8$ mm, where both satisfy the Fourier transform relationship. In this case, the joint uncertainty product $\Delta_{un} = 0.4113$. (d)–(f) JSA distribution when $L = 2$, 5, and 15 mm, respectively, with the corresponding $\Delta_{un} = 0.6413$, 0.2344, and 0.6801, respectively.

The nonlinear interaction strength of the nth pairwise spectral modes r_n is defined as $r_n = -i\gamma t\sqrt{\lambda_n}/\hbar$, as shown in Fig. 7(a) for the first ten compression coefficients. For simplicity, we set the squeezed angle $\theta = 0$. In our scheme, $\lambda_p = 780$ nm, $\omega_p = 2.41 \times 10^{15}$ rad/s, $\omega_s = \omega_i = 1.21 \times 10^{15}$ rad/s, the input pump power $P = 0.01$ mW, $n_p = 2.16$, $n_s = n_i = 1.99$, $S_{\text{eff}} = 176\,\text{mm}^2$, $L = 8$ mm, $\epsilon_k = n_k^2\epsilon_0$, and $\chi^{(2)} = 2d_{33}$, where $d_{33} = 25$ pm/V. Considering $\sum_n |\sqrt{\lambda_n}|^2 = 1$, the total squeezed amplitude $r = \gamma t/\hbar = 0.258$. As illustrated in Eq. (2), the generated two-mode squeezed state can be represented by the sum of the photon number state $|k, k\rangle$; the first ten coefficients $C_{k,k}$ are shown in Fig. 7(b). The von Neumann entropy defined as

$$S_r = -\sum_k P_k \ln(P_k) = -\sum_k \frac{(\tanh^2 r)^k}{\cosh^2 r} \ln\left(\frac{(\tanh^2 r)^k}{\cosh^2 r}\right) \tag{23}$$

is usually used to measure the degree of compression of the two-mode squeezed state. We plot $S_r(k)$ versus k for successive iterations in Fig. 7(c); $S_r(k)$ converges to 0.192, indicating the generated state has entanglement in the X-P DOF.

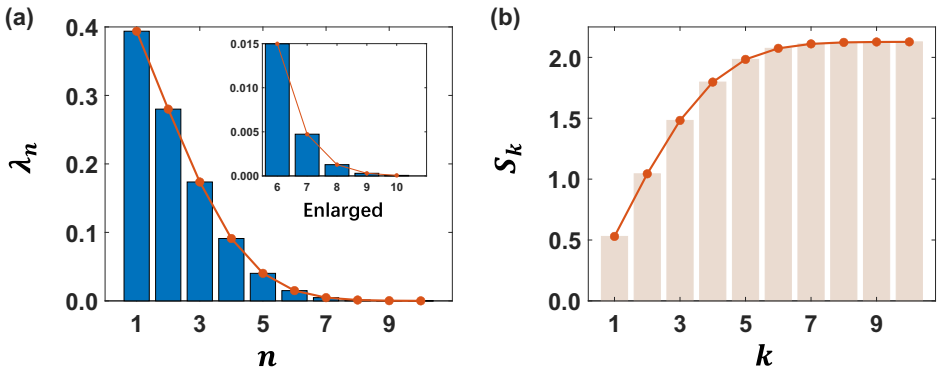

FIG. 6. (a) Maximum ten Schmidt coefficients after Schmidt decomposition of the JSA. The latter coefficients are close to 0, and their contributions to the entropy of entanglement S and the effective Schmidt rank K are negligible. (b) Entropy of entanglement S of our designed entanglement source. The results of successive iterations are shown, and S_k converges to 2.1276.

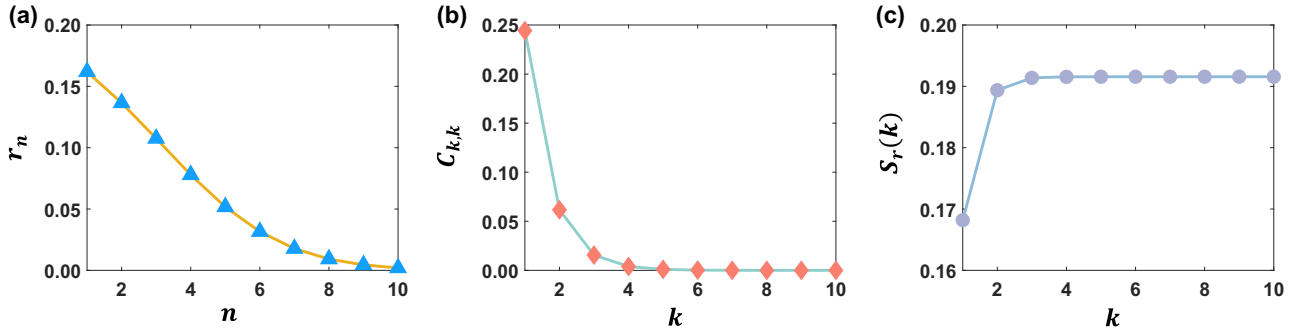

FIG. 7. (a) Squeezed coefficient r_n of each Schmidt orthogonal mode. We show only the first ten compression coefficients for simplicity. (b) First ten coefficients $C_{k,k}$ of the photon number state $|k,k\rangle$. (c) Squeezing degree S_r of the generated two-mode squeezed state, which finally reaches 0.192.

IV. APPLICATION

The multiplexing of multiple DOFs in the hyperentangled state enables higher-dimensional hyperentanglement-based QKD [34] and has the ability to achieve higher secret key rates, although the degree of entanglement in each DOF may be reduced (compared with the state entangled in only a single DOF). We apply our generated hyperentangled state to the theoretical free-space QKD system in Ref. [35], demonstrating its ability for high-dimensional encoding. The generalized d-dimensional QKD protocol consists of five procedures:

(1) Alice generates entangled photon pairs. Alice retains one photon from each entangled pair, while the other photon is sent to Bob via a quantum channel. This channel could be a fiber-optic cable or free-space transmission, depending on the specific implementation. The entanglement ensures that the photons remain correlated even after they are separated.

(2) Once Bob receives his photon, both Alice and Bob independently and randomly choose a set of mutually unbiased bases (MUBs) for measurement. Alice and Bob perform d-outcome measurements on their respective photons. The number of possible outcomes, d, depends on the dimension of the quantum system being used. For example, in a two-dimensional system (qubits), d would be 2, resulting in binary outcomes (0 or 1). In higher-dimensional systems, d could be larger, leading to d-ary symbols. Each measurement yields a d-ary symbol, which is recorded by Alice and Bob. These symbols are the raw data that will be used to generate the final secret key.

(3) After the measurements, Alice and Bob engage in a sifting process. They publicly reveal the MUBs they used for their measurements. This step is crucial because it allows them to identify which measurements were performed in the same basis. Only the symbols corresponding to pairs measured in the same MUB are retained, and all other symbols are discarded. The retained symbols form the sifted key, which is a preliminary version of the final secret key.

(4) To assess the security of the sifted key, Alice and Bob perform parameter estimation. They compare a subset of their sifted data to estimate the average error rate, denoted as Q. If Q is too high, it indicates that Eve may have intercepted and measured the photons, introducing errors in the data. In such cases, the protocol may abort or take additional security measures.

(5) On the basis of the estimated error rate Q, Alice and Bob proceed to generate the final secret key. This involves two critical steps: error correction and privacy amplification. After completing these steps, Alice and Bob are left with a final secret key that is secure and unknown to Eve. This key can be used for secure communication, such as encryption and decryption of messages, ensuring that the communication remains confidential and tamper-proof.

In the d-dimensional free-space QKD system using the photons that survive the postselection, the secret key rate can be expressed as [35]

$$R_{\text{key}} = \log_2 d + \frac{d+1}{d} Q \log_2 \frac{Q}{d(d-1)} + \left(1 - \frac{d+1}{d} Q\right) \log_2 \left(1 - \frac{d+1}{d} Q\right). \quad (24)$$

Figure 8 shows the variation of the secret key rate R_{key} with different dimension d when $Q = 0.05, 0.02, 0.01$, and 0.001. From Fig. 8, we can clearly see that the secret key rate R_{key} increases with increasing dimension d at constant error rate Q; for the implementation with a fixed dimension d, the secret key rate R_{key} approaches $\log_2 d$ when $Q \to 0$, which corresponds to the case of an ideal QKD system with no errors.

Just as traditional classical communication uses techniques such as polarization multiplexing, time division multiplexing, and quadrature amplitude modulation, in the field of quantum communication, our hyperentangled

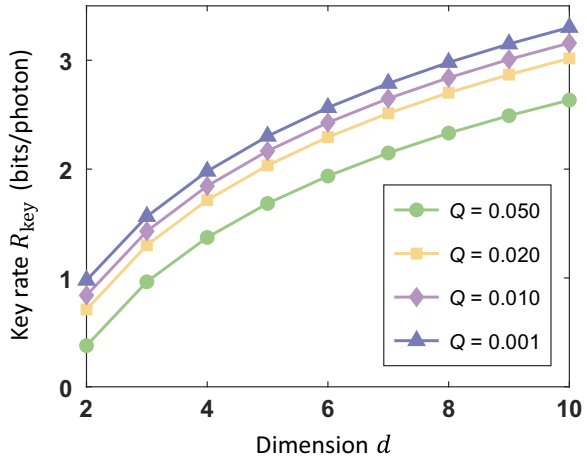

FIG. 8. Variation of secret key rate R_{key} with dimension d for different Q.

state also has the potential to combine these techniques to increase channel capacity and communication efficiency. In the polarization DOF, the bit information can be encoded on two orthogonal polarizations, such as $|H\rangle$ and $|V\rangle$, yielding the encoding subspace H_{pol} with dimension $d_{\text{pol}} = 2$. In the energy-time DOF, we can encode multiple bits per photon pair in their times of arrival. Each time frame with frame size T_f can be discretized into N time slots with time-bin duration τ ($T_f = N\tau$). The random arrival of coincident photon pairs is time-binned within an N-bin time frame, which yields a symbol comprising $\log_2 N$ bits [36]. Therefore, its Hilbert subspace H_{time} has the potential for encoding in higher dimensions ($d_{\text{time}} = N$). In the X-P DOF, similarly to the energy-time DOF, quadrature amplitude or phase can also be discretized into M parts to construct Hilbert subspace H_q with dimension $d_q = M$. Consequently, the whole encoding space $H_{\text{code}} = H_{\text{pol}} \bigotimes H_{\text{time}} \bigotimes H_q$ has the total dimension $d = d_{\text{pol}} \times d_{\text{time}} \times d_q = 2 \times M \times N$. According to the results from Fig. 8, our generated hyperentangled state can use more dimensions to represent information, thus increasing secret key rates and increasing the efficiency of quantum communication. Note that the QKD protocol using the squeezed state is more robust regrading channel excess noise and can tolerate higher channel loss, ensuring secure long-distance quantum communication [22]. Moreover, compared with the QKD protocol with high-dimensional encoding in only one DOF, the QKD protocol with simultaneous encoding in multiple DOFs in the hyperentangled state (which is called "hyperencoding") is more flexible, because the information encoding in multiple DOFs can be used to generate secret keys independently, and operational errors in one DOF will not affect the generation of secret keys in other DOFs [37,38]. However, the QKD system with excessively high dimensions often requires more complex quantum state preparation and measurement techniques, which may be more sensitive to noise and environmental interference, leading to higher error rates. Therefore, in the actual QKD system, it is necessary to choose the appropriate dimension d on the basis of specific application scenarios and experimental conditions.

V. CONCLUSION

We propose a compact scheme to generate a hyperentangled state in the polarization, energy-time, and quadrature amplitude-phase DOFs in a nanophotonic PPLN waveguide. The magnitude of the CHSH parameter $|S| = 2.375$, while the joint uncertainty product $\Delta(\omega_s + \omega_i)\Delta(t_s - t_i) = 0.4113$. Moreover, The von Neumann entropy S_r of the generated two-mode squeezed state can reach 0.192. Our proposed scheme for preparing hyperentangled states, which leverages the SPDC process and single-period poling in second-order nonlinear crystals, is generally applicable and not limited to lithium niobate. While the specific design and optimization details provided in this article are tailored for PPLN waveguides, the underlying concepts of quasi-phase-matching and hyperentanglement generation through SPDC can be adapted to other second-order nonlinear crystals, such as potassium titanyl phosphate, provided they meet the necessary phase-matching conditions and material properties. The key principle is to control dispersion by designing crystal structures to achieve quasi-phase-matching for manipulating multiple DOFs. Our approach could pave the way for high-capacity and high-speed quantum communication.

ACKNOWLEDGMENTS

This work was supported by the National Natural Science Foundation of China (Grant No. 62075129), the Open Project Program of the SJTU-Pinghu Institute of Intelligent Optoelectronics (Grant No. 2022SPIOE204), the Sichuan Provincial Key Laboratory of Microwave Photonics (Grant No. 2023-04) and the Science and Technology on Metrology and Calibration Laboratory (Grant No. JLKG2024001B002).

[1] J. T. Barreiro, N. K. Langford, N. A. Peters, and P. G. Kwiat, Generation of hyperentangled photon pairs, Phys. Rev. Lett. **95**, 260501 (2005).

[2] F. Graffitti, V. D'Ambrosio, M. Proietti, J. Ho, B. Piccirillo, C. de Lisio, L. Marrucci, and A. Fedrizzi, Hyperentanglement in structured quantum light, Phys. Rev. Res. **2**, 043350 (2020).

[3] J. H. Kim, Y. Kim, D. G. Im, C. H. Lee, J. W. Chae, G. Scarcelli, and Y. H. Kim, Noise-resistant quantum communications using hyperentanglement, Optica **8**, 1524 (2021).

[4] C. Xi, Y. Ding, B. Ji, X. Gong, and G. He, in *OSA Advanced Photonics Congress (AP) 2020 (IPR, NP, NOMA,*

Networks, PVLED, PSC, SPPCom, SOF) (Optica Publishing Group, Washington, DC United States, 2020) p. NpTu4D.11.

[5] J. Ouyang, Y. Liao, Z. Ma, D. Kong, X. Feng, X. Zhang, X. Dong, K. Cui, F. Liu, W. Zhang, *et al.*, On-demand photonic Ising machine with simplified Hamiltonian calculation by phase encoding and intensity detection, Commun. Phys. **7**, 168 (2024).

[6] Y. B. Sheng, F. G. Deng, and G. L. Long, Complete hyperentangled-Bell-state analysis for quantum communication, Phys. Rev. A **82**, 032318 (2010).

[7] Y. Tian, Y. Zhang, S. Liu, P. Wang, Z. Lu, X. Wang, and Y. Li, High-performance long-distance discrete-modulation continuous-variable quantum key distribution, Opt. Lett. **48**, 2953 (2023).

[8] J. Huang, X. Li, X. Chen, C. Zhai, Y. Zheng, Y. Chi, Y. Li, Q. He, Q. Gong, and J. Wang, Demonstration of hypergraph-state quantum information processing, Nat. Commun. **15**, 2601 (2024).

[9] A. K. Ekert, Quantum cryptography based on Bell's theorem, Phys. Rev. Lett. **67**, 661 (1991).

[10] C. Silberhorn, N. Korolkova, and G. Leuchs, Quantum key distribution with bright entangled beams, Phys. Rev. Lett. **88**, 167902 (2002).

[11] T. M. Graham, H. J. Bernstein, T. C. Wei, M. Junge, and P. G. Kwiat, Superdense teleportation using hyperentangled photons, Nat. Commun. **6**, 7185 (2015).

[12] X.-L. Wang, X.-D. Cai, Z.-E. Su, M.-C. Chen, D. Wu, L. Li, N.-L. Liu, C.-Y. Lu, and J.-W. Pan, Quantum teleportation of multiple degrees of freedom of a single photon, Nature **518**, 516 (2015).

[13] L. Ali, M. Ikram, T. Abbas, and I. Ahmad, Hyperentanglement teleportation through external momenta states, J. Phys. B: At. Mol. Opt. Phys. **54**, 235501 (2022).

[14] S. P. Walborn, A. H. Pimentel, L. Davidovich, and R. L. de Matos Filho, Quantum-enhanced sensing from hyperentanglement, Phys. Rev. A **97**, 010301 (2018).

[15] K. Wang, X. Wang, X. Zhan, Z. Bian, J. Li, B. C. Sanders, and P. Xue, Entanglement-enhanced quantum metrology in a noisy environment, Phys. Rev. A **97**, 042112 (2018).

[16] V. Trávníček, K. Bartkiewicz, A. Černoch, and K. Lemr, Experimental measurement of a nonlinear entanglement witness by hyperentangling two-qubit states, Phys. Rev. A **98**, 032307 (2018).

[17] L. Nemirovsky-Levy, U. Pereg, and M. Segev, Increasing quantum communication rates using hyperentangled photonic states, Opt. Quantum **2**, 165 (2024).

[18] Z. Xie, T. Zhong, S. Shrestha, X. Xu, J. Liang, Y.-X. Gong, J. C. Bienfang, A. Restelli, J. H. Shapiro, F. N. Wong, *et al.*, Harnessing high-dimensional hyperentanglement through a biphoton frequency comb, Nat. Photonics **9**, 536 (2015).

[19] X.-M. Hu, W.-B. Xing, B.-H. Liu, D.-Y. He, H. Cao, Y. Guo, C. Zhang, H. Zhang, Y.-F. Huang, C.-F. Li, and G.-C. Guo, Efficient distribution of high-dimensional entanglement through 11 km fiber, Optica **7**, 738 (2020).

[20] J. C. Chapman, T. M. Graham, C. K. Zeitler, H. J. Bernstein, and P. G. Kwiat, Time-bin and polarization superdense teleportation for space applications, Phys. Rev. Appl. **14**, 014044 (2020).

[21] P. Zhao, M.-Y. Yang, S. Zhu, L. Zhou, W. Zhong, M.-M. Du, and Y.-B. Sheng, Generation of hyperentangled state encoded in three degrees of freedom, Sci. China Phys. Mech. Astron. **66**, 100311 (2023).

[22] N. Wang, S. Du, W. Liu, X. Wang, Y. Li, and K. Peng, Long-distance continuous-variable quantum key distribution with entangled states, Phys. Rev. Appl. **10**, 064028 (2018).

[23] S. Saravi, T. Pertsch, and F. Setzpfandt, Generation of counterpropagating path-entangled photon pairs in a single periodic waveguide, Phys. Rev. Lett. **118**, 183603 (2017).

[24] Y.-H. Chen, Z. Jiang, and G.-Q. He, Generation of hyperentangled photon pairs based on lithium niobate waveguide, Chin. Phys. B **32**, 090306 (2023).

[25] Z. Zeng, S. You, Z. Yang, C. Yuan, C. You, and R. Jin, Controllable transitions among phase-matching conditions in a single nonlinear crystal, Chin. Opt. Lett. **22**, 021901 (2024).

[26] J. F. Clauser, M. A. Horne, A. Shimony, and R. A. Holt, Proposed experiment to test local hidden-variable theories, Phys. Rev. Lett. **23**, 880 (1969).

[27] R. A. Brewster, G. Baumgartner, and Y. K. Chembo, Quantum analysis of polarization entanglement degradation induced by multiple-photon-pair generation, Phys. Rev. A **104**, 022411 (2021).

[28] C. Law, I. A. Walmsley, and J. Eberly, Continuous frequency entanglement: Effective finite Hilbert space and entropy control, Phys. Rev. Lett. **84**, 5304 (2000).

[29] J.-P. W. MacLean, J. M. Donohue, and K. J. Resch, Direct characterization of ultrafast energy-time entangled photon pairs, Phys. Rev. Lett. **120**, 053601 (2018).

[30] Z. Zhang, C. Yuan, S. Shen, H. Yu, R. Zhang, H. Wang, H. Li, Y. Wang, G. Deng, Z. Wang, *et al.*, High-performance quantum entanglement generation via cascaded second-order nonlinear processes, npj Quantum Inf. **7**, 123 (2021).

[31] I. A. Khan and J. C. Howell, Experimental demonstration of high two-photon time-energy entanglement, Phys. Rev. A **73**, 031801 (2006).

[32] E. Rozenberg, A. Karnieli, O. Yesharim, J. Foley-Comer, S. Trajtenberg-Mills, D. Freedman, A. M. Bronstein, and A. Arie, Inverse design of spontaneous parametric downconversion for generation of high-dimensional qudits, Optica **9**, 602 (2022).

[33] X. Wang, T. Wu, C. Dong, H. Zhu, Z. Zhu, and S. Zhao, Integrating deep learning to achieve phase compensation for free-space orbital-angular-momentum-encoded quantum key distribution under atmospheric turbulence, Photonics Res. **9**, B9 (2021).

[34] J. C. Chapman, C. C. Lim, and P. G. Kwiat, Hyperentangled time-bin and polarization quantum key distribution, Phys. Rev. Appl. **18**, 044027 (2022).

[35] Z. Wang, R. Malaney, and B. Burnett, Satellite-to-earth quantum key distribution via orbital angular momentum, Phys. Rev. Appl. **14**, 064031 (2020).

[36] T. Zhong, H. Zhou, R. D. Horansky, C. Lee, V. B. Verma, A. E. Lita, A. Restelli, J. C. Bienfang, R. P. Mirin, T. Gerrits, *et al.*, Photon-efficient quantum key distribution using time–energy entanglement with high-dimensional encoding, New J. Phys **17**, 022002 (2015).

[37] Z.-X. Cui, W. Zhong, L. Zhou, and Y.-B. Sheng, Measurement-device-independent quantum key distribution with hyper-encoding, Sci. China Phys. Mech. Astron. **62**, 110311 (2019).

[38] Y.-F. Yan, L. Zhou, W. Zhong, and Y.-B. Sheng, Measurement-device-independent quantum key distribution of multiple degrees of freedom of a single photon, Front. Phys. **16**, 11501 (2021).